ANNUAL REVIEWS

Coherently Coupled Mixtures of Ultracold Atomic Gases

Alessio Recati[1,2] and Sandro Stringari[1,2]

[1]Istituto Nazionale di Ottica–Consiglio Nazionale delle Ricerche (INO-CNR) Bose–Einstein Condensation (BEC) Center, Dipartimento di Fisica, Università di Trento, Povo, Italy; email: alessio.recati@unitn.it

[2]Trento Institute for Fundamental Physics and Applications, Istituto Nazionale di Fisica Nucleare (INFN), Povo, Italy

ANNUAL REVIEWS CONNECT

www.annualreviews.org

- Download figures
- Navigate cited references
- Keyword search
- Explore related articles
- Share via email or social media

Keywords

spinor Bose–Einstein condensates, superfluidity, magnetism, spin–orbit coupling

Abstract

This article summarizes some of the relevant features exhibited by binary mixtures of Bose–Einstein condensates in the presence of coherent coupling at zero temperature. The coupling, which is experimentally produced by proper photon transitions, can involve either negligible momentum transfer from the electromagnetic radiation (Rabi coupling) or large momentum transfer (Raman coupling) associated with spin–orbit effects. The nature of the quantum phases exhibited by coherently coupled mixtures is discussed in detail, including their paramagnetic, ferromagnetic, and, in the case of spin–orbit coupling, supersolid phases. The behavior of the corresponding elementary excitations is discussed, with explicit emphasis on the novel features caused by the spin-like degree of freedom. Focus is further given to the topological excitations (solitons, vortices) as well as to the superfluid properties. This review also points out relevant open questions that deserve more systematic theoretical and experimental investigations.

1. INTRODUCTION

Since the first experimental realization of Bose–Einstein condensation in cold gases of alkali atoms (1, 2), the investigation of quantum mixtures (3) has become a very popular subject of research in atomic physics, stimulating extensive theoretical and experimental activity of both fundamental and applicative interest. Important achievements have concerned, among others, the realization of novel quantum phases, the study of collective dynamics and solitonic configurations, the realization of polar molecules, and the formation of quantum droplets. First experiments focused on alkali-metal gases, but there is currently a growing interest in mixtures composed of different atomic species, including Bose–Bose, Bose–Fermi, and Fermi–Fermi mixtures. These studies, reported by an impressive number of scientific works, represent the systematic implementation of the pioneering studies on quantum degenerate mixtures realized with helium fluids (4, 5).

An intriguing possibility is given by the creation of coherent coupling among the different atomic species forming the mixture, giving rise to novel scenarios for nontrivial equilibrium and nonequilibrium many-body configurations. The aim of this paper is to summarize some of the most salient features exhibited by these configurations. For simplicity, we limit our discussion to the case of quantum mixtures occupying two different hyperfine states, hereafter called $|\uparrow\rangle$ and $|\downarrow\rangle$. Employing the usual spin $s = 1/2$ representation these two single-particle states are classified as eigenstates of the Pauli matrix operator, σ_z, according to $\sigma_z|\uparrow\rangle = +|\uparrow\rangle$ and $\sigma_z|\downarrow\rangle = -|\downarrow\rangle$. The transfer of atoms between the two hyperfine states can be induced by proper photon transitions. Within the rotating wave approximation and using a suitable polarization of the electromagnetic radiation, the relevant single-particle spinor Hamiltonian takes the following form:

$$h_{sp} = \frac{\mathbf{p}^2}{2m} - \frac{\hbar\Omega}{2}\sigma_x \cos(2k_0 x - \Delta\omega_L t) - \frac{\hbar\Omega}{2}\sigma_y \sin(2k_0 x - \Delta\omega_L t) + \frac{\hbar\Delta\omega_{hf}}{2}\sigma_z, \qquad 1.$$

where $\mathbf{p}$ is the canonical momentum, Ω (hereafter assumed real and positive) defines the intensity of the coupling of the atoms with the electromagnetic field, k_0 is the modulus of the wave vector difference between the two electromagnetic fields (hereafter chosen to be counter propagating along the x direction), and $\Delta\omega_L$ is the corresponding frequency difference. The energy $\hbar\Delta\omega_{hf}$ is the energy difference between the two hyperfine states, including the nonlinear Zeeman effect.

In the following, we distinguish the case in which one can neglect the momentum transfer ($k_0 = 0$), which we refer to as Rabi coupling, from the case in which the value of k_0 cannot be ignored, which we refer to as Raman (or spin–orbit) coupling (SOC).

The Hamiltonian (Equation 1) is not translational invariant, but exhibits a peculiar continuous screw-like symmetry, being invariant with respect to helicoidal translations of the form $\exp[id(p_x - \hbar k_0\sigma_z)/\hbar]$, consisting of the combination of a rigid translation with displacement d and a spin rotation by the angle $-2dk_0$ around the z axis. Translational invariance is obviously recovered for the Rabi coupling case.

The Hamiltonian (Equation 1) can be made time-independent and translational invariant by going to the so-called laser reference frame through the unitary transformation $U = \exp(i\Theta\sigma_z/2)$, corresponding to a position and time-dependent rotation in spin space by the angle $\Theta = 2k_0 x - \Delta\omega_L t$. The new Hamiltonian $h \to Uh_{sp}U^\dagger + i\hbar\dot{U}U^\dagger$ acquires the form

$$h_{Rabi} = \frac{\mathbf{p}^2}{2m} - \frac{\hbar\Omega}{2}\sigma_x + \frac{\hbar\delta}{2}\sigma_z, \qquad 2.$$

$$h_{SOC} = \frac{1}{2m}\left[(p_x - \hbar k_0\sigma_z)^2 + p_\perp^2\right] + \frac{\hbar\Omega}{2}\sigma_x + \frac{\hbar\delta}{2}\sigma_z, \qquad 3.$$

where, for later convenience, we have introduced the Rabi Hamiltonian h_{Rabi} for $k_0 = 0$ and the spin–orbit Hamiltonian h_{SOC} for $k_0 \neq 0$, and the detuning $\delta = \Delta\omega_{\mathrm{L}} - \Delta\omega_{\mathrm{hf}}$ is due to the additional time dependence of the unitary transformation. The spin–orbit term in Equation 3 results from the noncommutativity between the kinetic energy and the position-dependent rotation. The spin–orbit Hamiltonian of Equation 3 is characterized by equal Rashba (6) and Dresselhaus (7) strengths. It is worth noticing that the canonical momentum $p_x = -i\hbar\partial_x$ entering the spin–orbit Hamiltonian does not coincide with the physical momentum of particles, because of the presence of the spin term $\hbar k_0 \sigma_z$. It is also useful to remark that the unitary transformation U affects neither the density $n(\mathbf{r}) = n_\uparrow(\mathbf{r}) + n_\downarrow(\mathbf{r})$ nor the z component $s_z(\mathbf{r}) = n_\uparrow(\mathbf{r}) - n_\downarrow(\mathbf{r})$ of the spin density. These quantities can be consequently safely calculated in the spin rotated frame, using the Hamiltonian (Equation 3).

In the following, we consider bosonic species that naturally undergo Bose–Einstein condensation at sufficiently low temperature and can reveal peculiar coherence effects associated with the Hamiltonians discussed above. In the weakly interacting regime, a three-dimensional (3D) quantum mixture of bosonic atoms interacting with short-range interactions is well described by mean-field (MF) theory, where the state of the system is conveniently described by a two-component spinor wave function $\Psi(\mathbf{r}, t) = [\Psi_\uparrow(\mathbf{r}, \mathbf{t}), \Psi_\downarrow(\mathbf{r}, \mathbf{t})]^T$, normalized to the total number of particles $\int d\mathbf{r}\Psi^\dagger\Psi = N$, while the total energy of the system, including both single-particle and interaction terms, can be expressed in terms of the relevant coupling constants as

$$E = \int d\mathbf{r}\varepsilon_{\mathrm{MF}} = \int d\mathbf{r}\left[\Psi^\dagger h_{\mathrm{sp}}\Psi + \frac{g_{\mathrm{dd}}}{2}n^2 + \frac{g_{\mathrm{ss}}}{2}s_z^2\right], \qquad 4.$$

where $n = \Psi^\dagger\Psi$ and $s_z = \Psi^\dagger\sigma_z\Psi$ are the total and spin density, respectively. The density–density and spin–spin coupling constants are given by $g_{\mathrm{dd}} = (g + g_{\uparrow\downarrow})/2$ and $g_{\mathrm{ss}} = (g - g_{\uparrow\downarrow})/2$, respectively and, for simplicity, we have assumed that the intraspecies couplings are equal, i.e., $g_{\uparrow\uparrow} = g_{\downarrow\downarrow} \equiv g > 0$ and $g_{\mathrm{dd}} > 0$, to assure MF stability against collapse. The most general case would include different intraspecies couplings. In this case, one should replace g with $(g_{\uparrow\uparrow} + g_{\downarrow\downarrow})/2$ and add a third term $g_{\mathrm{ds}}ns_z$, with $g_{\mathrm{ds}} = (g_{\uparrow\uparrow} - g_{\downarrow\downarrow})/4$ inside the integral of Equation 4. The couplings in each channel are related to the corresponding s-wave scattering lengths via $g_{\sigma\sigma'} = 4\pi\hbar^2 a_{\sigma\sigma'}/m$.

Starting from the energy functional (Equation 4), one can derive coupled Gross–Pitaevskii equations for the separate components of the spinor wave function, whose predictions are discussed in the next sections.

For reasons of space, we are unable to discuss here important results concerning coherently coupled mixtures in which the MF description is not appropriate, like, for example, the case of large enough attractive interspecies interaction, beyond which MF Lee–Huang–Yang corrections become crucially important (8) and even yield self-bound droplet states (9–12), and the case of cold gases trapped in a deep optical lattice in which the system is properly described by Bose-Hubbard-like Hamiltonians allowing for strongly correlated configurations (see, e.g., 13–18).

2. DISCRETE AND CONTINUOUS SYMMETRIES

The Hamiltonians discussed in the previous section exhibit important symmetries that are worth discussing because they permit us to better understand the nature of the new equilibrium phases as well as the novel dynamic and superfluid features caused by Rabi and SOC.

Let us first consider the relevant discrete symmetries exhibited by our mixtures. $\mathbb{Z}_2$ is an important symmetry reflecting, for vanishing detuning, the symmetry of the Hamiltonian with respect to the exchange of the coordinates of the two components. This symmetry is preserved in the presence of the most relevant term proportional to $\Omega\sigma_x$. The spontaneous breaking of the

$\mathbb{Z}_2$ symmetry is at the origin of the ferromagnetic phases exhibited in the presence of both Rabi and SOC, although the underlying mechanisms are different in the two cases (see Sections 3.1 and 4.2). Another important case of discrete symmetries concerns time reversal and parity. They are both violated by the spin–orbit Hamiltonian (Equation 3) with crucial consequences on the breaking of the symmetry property $\omega(q) = \omega(-q)$ usually exhibited by the spectrum of the elementary excitations (see Section 4.3).

An important consequence of the term proportional to Ω in the Hamiltonian is the violation of the continuous symmetry with respect to the relative phase $\phi_r = \phi_\uparrow - \phi_\downarrow$ of the order parameters of the two spin states. This is well understood by writing the two order parameters in the form $\Psi_\uparrow = \sqrt{n_\uparrow} \exp(i\phi_\uparrow)$ and $\Psi_\downarrow = \sqrt{n_\downarrow} \exp(i\phi_\downarrow)$. The expectation value $E_\Omega = \langle H_\Omega \rangle$ of the operator $H_\Omega = -(\hbar\Omega/2)\sigma_x$ then takes the form

$$E_\Omega = -\frac{\hbar\Omega}{2} \int d\mathbf{r}(\Psi_\uparrow^* \Psi_\downarrow + \Psi_\uparrow^* \Psi_\downarrow) = -\hbar\Omega \int d\mathbf{r}\sqrt{n_\uparrow n_\downarrow} \cos\phi_r, \qquad 5.$$

which depends explicitly on the relative phase ϕ_r. The breaking of this symmetry, which in the absence of Rabi or Raman coupling would add to the U(1) symmetry associated with the total phase of the two order parameters, has deep consequences on the dispersion of the spin excitations, causing the appearance of a gap (see Sections 3.2 and 4.3). The dependence of E_Ω on the relative phase also implies that the relative number $N_\uparrow - N_\downarrow = \langle \sum_j \sigma_{zj} \rangle$ of atoms in the two spin states is not conserved and obeys the following equation:

$$\frac{d(N_\uparrow - N_\downarrow)}{dt} = \frac{1}{i\hbar} \left\langle \left[\sum_j \sigma_{zj}, H_\Omega \right] \right\rangle = \Omega \int d\mathbf{r}\sqrt{n_\uparrow n_\downarrow} \sin\phi_r. \qquad 6.$$

The ground state of the mixture corresponds to the condition of equal phases ($\phi_\uparrow = \phi_\downarrow$) and, hence, to a stationary value of $N_\uparrow - N_\downarrow$. Out of equilibrium, the relative number of atoms can instead exhibit time-dependent oscillations (19), corresponding to the so-called internal Josephson effect (see Section 3.3). The new topology imposed by the relative phase dependence of E_Ω also has important consequences on the nature of the solitonic solutions as well as on the rotational properties of the system and, in particular, on the behavior of the vortex lines (see Section 3.4).

Both the Rabi and the spin–orbit Hamiltonians (Equations 2 and 3) are translational invariant and commute with the canonical momentum $p_x = -i\hbar\partial_x$. In the case of SOC the translational invariance can be spontaneously broken, giving rise to a peculiar stripe (ST) phase, with characteristic supersolid features (see Section 4.2). Translational invariance is not, however, equivalent to Galilean invariance, which is explicitly violated by the spin–orbit Hamiltonian. This is best understood by calculating how the spin–orbit Hamiltonian (Equation 3) is transformed by the unitary Galilean transformation $G = \exp(imvx/\hbar)$, which provides a Galilean boost, corresponding to the displacement mv of the wave function in momentum space, along the x direction. Only the x component of the kinetic energy term is modified by the Galilean transformation and takes the form $G^{-1}(px - \hbar k_0\sigma_z)^2 G/2m = (p_x - \hbar k_0\sigma_z + mv)^2/2m$ so that, in the new frame, the spin–orbit Hamiltonian $h'_{\text{SOC}} = G^{-1}h_{\text{SOC}}G$ is given by

$$h'_{\text{SOC}} = h_{\text{SOC}} + \frac{m}{2}v^2 + mv(p_x - \hbar k_0\sigma_z). \qquad 7.$$

The operator $(px - \hbar k_0\sigma_z)$, which represents the physical momentum of the particle, is not a constant of motion, because of the presence of the Raman coupling $\Omega\sigma_x$ in the spin–orbit Hamiltonian. As a consequence, the two Hamiltonians h'_{SOC} and h_{SOC} are physically different, yielding a violation of Galilean invariance with important consequences on the superfluid properties of the system, as discussed in Section 4.4.

3. EQUILIBRIUM AND NONEQUILIBRIUM PROPERTIES OF RABI COUPLED GASES

In this section, we describe the phase diagram, the elementary excitations, and some topological configurations, as well as far-from-equilibrium properties of a spinor condensate in the presence of Rabi coupling. The system has been thoroughly studied theoretically at the MF level (see 20 and references therein), with the first studies dating back to the 1990s (21, 22). The first experimental realization was obtained in the group of Eric Cornell (23, 24) with the aim of studying superfluidity in the presence of spinor configurations.

3.1. Ground State Properties

In the following, we mainly consider the case $\delta = 0$, ensuring $\mathbb{Z}_2$ symmetry. In this case, the MF energy density of a homogeneous gas reads

$$\varepsilon_{\text{MF}} = \frac{g_{\text{dd}}}{2}n^2 + \frac{g_{\text{ss}}}{2}s_z^2 - \frac{\Omega}{2}\sqrt{n^2 - s_z^2}\cos(\phi_r), \qquad 8.$$

with $n = N/V$. The stationary states are found by minimizing the grand canonical energy density $\varepsilon_{\text{MF}} - \mu n$ with respect to n, s_z, and ϕ_r, where μ is the chemical potential. The ground state is characterized by the vanishing of the relative phase ($\phi_r = 0$) and obeys the coupled equations

$$\mu = g_{\text{dd}}n - \frac{\Omega n}{2\sqrt{n^2 - s_z^2}}, \qquad 9.$$

$$0 = g_{\text{ss}}s_z + \frac{\Omega s_z}{2\sqrt{n^2 - s_z^2}}, \qquad 10.$$

exhibiting a bifurcation (see **Figure 1**) as a function of Ω. Although for $\Omega > -2g_{\text{ss}}n$ the ground state solution has vanishing spin polarization, for smaller values of Ω, requiring the condition $g_{\text{ss}} < 0$, the lowest energy solution corresponds to a typical ferromagnetic configuration with spin polarization,

$$s_z = \pm n\sqrt{1 - \left(\frac{\Omega}{2g_{\text{ss}}n}\right)^2}. \qquad 11.$$

The transition between the two regimes is reminiscent of the quantum phase transition of the Ising model in transverse field (see, e.g., 25), and for this reason the two states are referred to as paramagnetic and ferromagnetic phases, respectively. The condition $\Omega + 2g_{\text{ss}}n = 0$ identifies the critical transition point. In the ferromagnetic phase, the system selects one of the two polarizations, spontaneously breaking the $\mathbb{Z}_2$ symmetry, and the polarization, close to the critical point, grows like $s_z \propto [-(2g_{\text{ss}}n + \Omega)]^\beta$, with the typical MF critical exponent $\beta = 1/2$. Also, the magnetic susceptibility $\chi = (\partial^2 \varepsilon_{\text{MF}}/\partial s_z^2)^{-1}$ exhibits the ferromagnetic behavior, diverging near the critical point at $\Omega + 2g_{\text{ss}}n = 0$. In the paramagnetic (P) and ferromagnetic (F) phases one finds

$$\chi_{\text{P}} = \frac{2n}{2g_{\text{ss}}n + \hbar\Omega}, \qquad 12.$$

$$\chi_{\text{F}} = \frac{(\hbar\Omega)^2}{|g_{\text{ss}}|}\frac{1}{(2g_{\text{ss}}n)^2 - (\hbar\Omega)^2}, \qquad 13.$$

respectively. In the absence of Rabi coupling the situation is very different because the total polarization $S_z = N_\uparrow - N_\downarrow$ is a conserved quantity, leading to a further U(1) symmetry of the
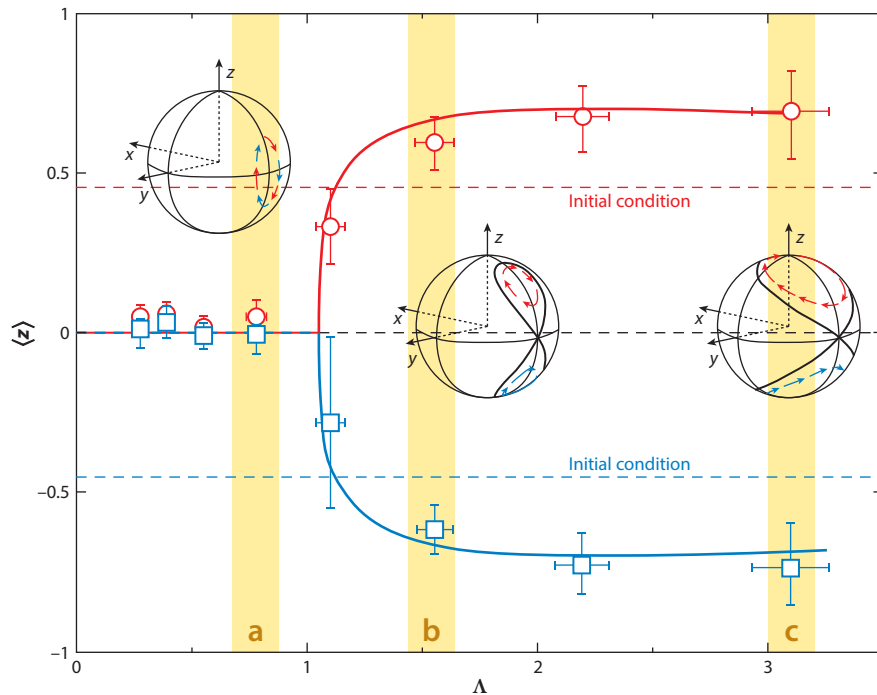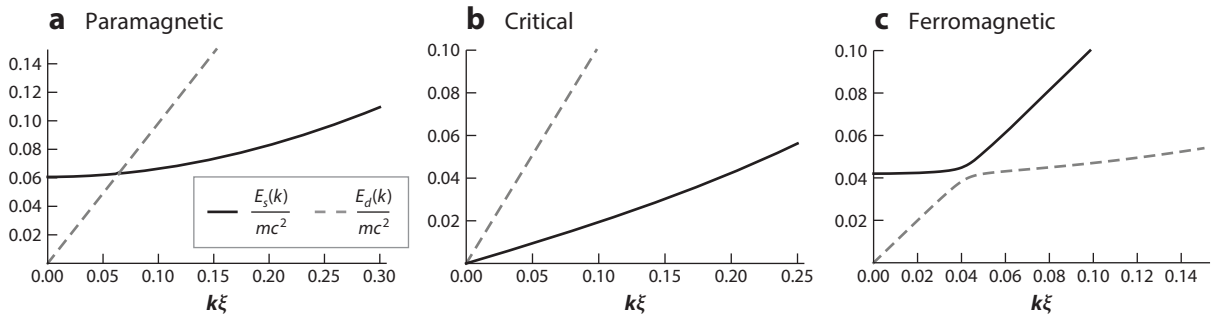
Figure 1

First experimental evidence of ferromagnetic-like bifurcation in a Rabi coupled gas of ^{87}Rb atoms. The total
relative magnetization $Z = (N_\uparrow - N_\downarrow)/(N_\uparrow + N_\downarrow)$ is plotted as a function of the ratio Λ, between the
magnetic interaction energy and the Rabi coupling (see Section 3.3). The Bloch spheres represent the
dynamics around the fixed points of the Bose–Josephson junction (Equation 28). In the experiment, the gas
was initially prepared with a positive (*red dashed line*) or negative (*blue dashed line*) polarization. In the Rabi
regime (*shaded region a*), both initial states share the same trajectory around the stable fixed point, and the
temporal mean imbalance vanishes. By increasing Λ to exceed the critical value, a separatrix is formed and
the chosen initial preparations lead to two distinct trajectories (*shaded regions b and c*) separated by this
separatrix. The dynamical modes are characterized by a nonvanishing mean population imbalance.
For $\Lambda < 2$, the phase oscillates around π, whose dynamics is reported in the Bloch sphere corresponding to
the points in shaded region b. For $\Lambda > 2$, the separatrix encloses the poles and the dynamics can show a
running phase behavior (Bloch sphere for the *points* in *shaded region c*). Figure adapted with permission
from 26; copyright 2010 American Physical Society.

Hamiltonian. In this case, the two ground states correspond to the miscible phase if $g_{ss} > 0$ (all
the atoms occupy the same volume) and exhibit immiscibility if $g_{ss} < 0$, in which case the two
atomic species occupy distinct regions in space. At zero temperature, an abrupt transition occurs
as soon as the coupling constant g_{ss} becomes negative.

The first experimental measurement of the transition between a para- and a ferromagnetic
phase in Rabi coupled gases was reported by the group of Markus Oberthaler (26, 27; see
Figure 1).

3.2. Elementary Excitations of a Rabi Coupled Bose–Einstein Condensed Mixture

Once the ground state is known, the excitations of the system are determined by Bogoliubov the-
ory. The Bogoliubov approach is known to be equivalent to the solution of the linearized equations

a Paramagnetic **b** Critical **c** Ferromagnetic

Figure 2

Spectrum of a Rabi coupled gas in the (*a*) paramagnetic and (*c*) ferromagnetic phases, and at the (*b*) critical point $\Omega + 2g_{ss}n = 0$.

of time-dependent Gross–Pitaevskii theory (see, e.g., 28). In a quantum mixture, the equations for the elementary excitations are more involved than in the single-component case, and for a more complete discussion we refer the interested reader to, e.g., References 20 and 29.

In **Figure 2**, we report the typical form of the spectrum across the ferromagnetic transition. The spectrum has two branches, which are usually referred to as density [$E_d(k)$] and spin [$E_s(k)$] branches. The branch $E_d(k)$ is gapless, and its low-energy behavior is dictated by the existence of the Goldstone mode due to the spontaneous breaking of the U(1) symmetry related to the conservation of the total number of particles. At low momenta it has a phonon-like behavior $E_d = c_d k$, with c_d being the speed of density sound. The branch $E_s(k)$ is instead gapped, as a consequence of the cost associated with the change of the relative phase ϕ_r. This cost is enforced by the Rabi coupling that explicitly breaks the symmetry U(1) relative to the conservation of the relative atomic population, which is different from what happens in standard Bose–Bose mixtures (i.e., in the absence of Rabi coupling), where the spin branch is also gapless (30). According to the theory of second-order phase transitions, the gap closes at the critical point and has a different behavior in the two phases (25). We find

$$\Delta_P = \sqrt{2n\hbar\Omega\chi_P^{-1}} \rightarrow \left[\hbar\Omega(2g_{ss}n + \hbar\Omega)\right]^{1/2} \quad \text{for } 2g_{ss}n + \hbar\Omega \rightarrow 0^+, \qquad 14.$$

$$\Delta_F = \sqrt{\frac{2(\hbar\Omega)^2}{|g_{ss}|}\chi_F^{-1}} \rightarrow \left[(2\hbar\Omega|2g_{ss}n + \hbar\Omega|)\right]^{1/2} \quad \text{for } 2g_{ss}n + \hbar\Omega \rightarrow 0^-, \qquad 15.$$

where we can identify the critical exponent for the gap that, within the present MF theory, coincides with the exponent $\beta = 1/2$ for the magnetization close to the critical point (see Equation 11). At the critical point the dispersion relation becomes linear with the speed of spin sound, given by $c_s = \sqrt{|g_{ss}|n/m}$. Notice that the spin spectrum for a standard Bose–Bose mixture becomes instead quadratic at the transition point to the immiscible regime, whereas in the phase separated regime the concept of spin sound does not make sense anymore.

Although the spin spectrum is gapless both for $\Omega = 0$ and at the critical point $\hbar\Omega = -2g_{ss}n$, the quantum fluctuations associated with the corresponding long wavelength modes behave very differently in the two cases. For $\Omega = 0$, the linear low-k energy mode is dominated by the fluctuations of the relative phase. However, at the critical point the low-energy mode is dominated by the fluctuations of the relative population (polarization), reflecting the critical nature of the ferromagnetic transition, as we discuss below.

In the unbroken $\mathbb{Z}_2$ paramagnetic phase, the Bogoliubov predictions for the dispersion law and for the corresponding quantum fluctuations take a particularly simple and instructive form. In this phase, the fluctuations of the total density (Π_d) and spin density (Π_s) operators as well as of the total phase (ϕ_d) and relative phase (ϕ_r) operators can be explicitly written in terms of the annihilation (creation) operators $d_{\mathbf{k}}$ ($d_{\mathbf{k}}^{\dagger}$) and $s_{\mathbf{k}}$ ($s_{\mathbf{k}}^{\dagger}$) for the density and spin excitations, respectively, as

$$\Pi_\alpha(\mathbf{r}) = \frac{\sqrt{n}}{2} \sum_{\mathbf{k}} (U_{\alpha,k} + V_{\alpha,k})(\alpha_{\mathbf{k}} e^{i\mathbf{k}\cdot\mathbf{r}} + \alpha_{\mathbf{k}}^{\dagger} e^{-i\mathbf{k}\cdot\mathbf{r}}) \qquad 16.$$

and

$$\phi_\alpha(\mathbf{r}) = i\sqrt{\frac{1}{2n}} \sum_{\mathbf{k}} (U_{\alpha,k} + V_{\alpha,k})^{-1}(\alpha_{\mathbf{k}} e^{i\mathbf{k}\cdot\mathbf{r}} - \alpha_{\mathbf{k}}^{\dagger} e^{-i\mathbf{k}\cdot\mathbf{r}}), \qquad 17.$$

where $\alpha = d$ and s, and $\mathbf{k}$ is the momentum of the corresponding excitations. In the above equations, we have introduced the so-called Bogoliubov amplitudes, Us and Vs, whose combination provides the contribution of each mode to the static structure factor according to $S_\alpha \propto |U_{\alpha,k} + V_{\alpha,k}|^2$. The proper diagonalization of the Bogoliubov Hamiltonian yields the following results for the Bogoliubov amplitudes of the density and spin excitations:[1]

$$U_{d,k} + V_{d,k} = \left(\frac{k^2}{k^2 + 8mg_d n}\right)^{\frac{1}{4}}, \quad U_{s,k} + V_{s,k} = \left[\frac{k^2 + 2m\hbar\Omega}{k^2 + 4m(2g_{ss}n + \hbar\Omega)}\right]^{\frac{1}{4}}. \qquad 18.$$

Analogously, one finds the following expressions for the dispersion laws:

$$E_d(k) = \sqrt{\frac{\hbar^2 k^2}{2m}\left(\frac{\hbar^2 k^2}{2m} + 2g_{dd}n\right)}, \qquad 19.$$

$$E_s(k) = \sqrt{\left(\frac{\hbar^2 k^2}{2m} + \hbar\Omega\right)\left(\frac{\hbar^2 k^2}{2m} + 2g_{ss}n + \hbar\Omega\right)}, \qquad 20.$$

allowing, in the $k \to 0$ limit, for the identification of the density sound velocity $c_d = \sqrt{g_{dd}n/m}$ and of the spin gap $\sqrt{\hbar\Omega(2g_{ss}n + \hbar\Omega)}$.

When $\Omega = 0$ and $g_{ss} > 0$ the Bogoliubov amplitudes in both the density and spin channels have the same structure as that for the single-component Bose gas and, as $k \to 0$, the fluctuations of the phase diverge while the static structure factors vanish linearly due to atom number conservation in each component.

If $\Omega > 0$, the spin channel instead reveals a very different behavior. The phase and amplitude mode are generally comparable also in the long wavelength limit, corresponding to a finite value of the spin static structure factor at low momenta. More importantly, at the critical point the fluctuations of the spin density become critically large, providing the k^{-1} divergent behavior of the spin structure factor, which is consistent with the divergent behavior of the magnetic polarizability (Equation 12). Such critical behavior of the spin fluctuations has been predicted to lead to a strong damping of the (density) Goldstone phonons. Indeed, while the Bogoliubov approach predicts an infinite lifetime for the elementary excitations, the phonon modes can decay into two

---

[1]See Reference 29 for the most general case, $g_{sd} \neq 0$.

lower-energy phonons leading to the so-called Belyaev damping, which scales as $\Gamma_{ddd}(k) \to k^5$ at small momenta. By contrast, the closing of the gap opens a new decay channel, in which a density mode can decay into two spin modes, yielding an enhanced damping that scales as $\Gamma_{dss}(k) \to k$ (31).

3.3. Hydrodynamic Formulation and Internal Josephson Effect

In the previous sections, we have discussed the ground state properties of Rabi coupled gases and the small amplitude oscillations around equilibrium. We provide a more general description of the MF dynamics of the spinor gas by developing the hydrodynamic formulation of the Gross–Pitaevskii equations. This formulation emphasizes in an explicit way the role of the spin density. In $s = 1/2$ spinors, the spin density components are defined by $s_i(\mathbf{r}) = (\Psi_\uparrow^*, \Psi_\downarrow^*)\sigma_i(\Psi_\uparrow, \Psi_\downarrow)^T$, with σ_i $(i = x, y, z)$ being the Pauli matrices. In particular, $s_x = \sqrt{n^2 - s_z^2}\cos\phi_r$ and $s_y = \sqrt{n^2 - s_z^2}\sin\phi_r$, and the relation $|\mathbf{s}(\mathbf{r})| = n(\mathbf{r})$ holds. The velocity field, defined as the total current divided by the density, takes the simple form

$$\mathbf{v}(\mathbf{r}) = \frac{\mathbf{j}(\mathbf{r})}{n} = \frac{\hbar}{2mni}\sum_{\sigma=\uparrow,\downarrow}(\Psi_\sigma^*\nabla\Psi_\sigma - \Psi_\sigma\nabla\Psi_\sigma^*) = \frac{\hbar}{2m}(\nabla\phi_d + s_z/n\,\nabla\phi_r), \qquad 21.$$

where $\phi_{d(r)} = \phi_\uparrow \pm \phi_\downarrow$ is the total (relative) phase. Due to the spinor nature of the wave function, the velocity field $\mathbf{v}(\mathbf{r})$ is not in general irrotational, but satisfies the relation $\nabla \times v = \hbar/(2m)\nabla(s_z/n) \times \nabla\phi_r$, corresponding to the analog of the Mermin–Ho relation (32), originally introduced for describing the superfluid A phase of ^{3}He. Eventually the hydrodynamics equations can be written as (see, e.g., 33)

$$\dot{n} + \mathrm{div}(n\mathbf{v}) = 0, \qquad 22.$$

$$m\dot{\mathbf{v}} + \nabla\left(\frac{mv^2}{2} + \mu + \frac{s_z}{n}h + V - \frac{\hbar^2\nabla^2\sqrt{n}}{2m\sqrt{n}} + \frac{\hbar^2|\nabla\mathbf{s}|^2}{8mn^2}\right) = 0, \qquad 23.$$

$$\dot{\mathbf{s}} + \sum_{\alpha=x,y,z}\partial_\alpha(\mathbf{j}_{s,\alpha}) = \mathbf{H}(\mathbf{s}) \times \mathbf{s}, \qquad 24.$$

where, for completeness, we have included a possible external trapping potential V.

The first equation is the standard continuity equation for the particle number conservation, and the second equation is the Euler equation, with the chemical potential μ and the internal magnetic field h given by

$$\mu = g_{dd}n - \frac{\hbar\Omega}{2}\frac{n}{n^2 - s_z^2}s_x,$$
$$h = g_{ss}s_z + \frac{\hbar\Omega}{2}\frac{s_z}{n^2 - s_z^2}s_x. \qquad 25.$$

Notice that there is no problem with the limiting case $s_z \to \pm n$, i.e., a fully polarized mixture since the term $\mu + hs_z/n = g_{dd}n + g_{ss}s_z + \hbar\Omega s_x/(2n)$ entering in the second Euler equation is well defined for any s_z. In the lower-energy states, where $s_x = \sqrt{n^2 - s_z^2}$ and $h = 0$, the above equations reduce to Equations 9 and 10, and the corresponding susceptibilities are given by $\chi^{-1} = \partial h/\partial s_z$. As pointed out in Reference 33, despite the possible presence of rotational components in the velocity field $\mathbf{v}$, the time derivative $\dot{\mathbf{v}}$ turns out to be irrotational.

The last equation (Equation 24) is the most interesting one, because it determines the spin dynamics. The left-hand side is the continuity equation, due to the Noether theorem for the

SU(2) symmetry. The spin current contains two contributions:

$$\mathbf{j}_{s,\alpha} = v_\alpha \mathbf{s} - \frac{\hbar}{2m}\left(\frac{\mathbf{s}}{n} \times \partial_\alpha \mathbf{s}\right), \quad \alpha = x, y, z, \qquad\qquad 26.$$

the first term being the classical spin advection and the second one corresponding to the spin–twist, whose contribution to the equation of motion is called quantum torque. In our system, the SU(2) symmetry is reduced to the $\mathbb{Z}_2$ symmetry by the effective field $\mathbf{H(s)} = (-\Omega, 0, 2g_{ss}s_z/\hbar)$, which enters the right-hand side of Equation 24.

If the dynamics involves neither the density nor the velocity, the system is described only by the spin (Equation 24). In this case, the equation of motion for a coherently coupled Bose–Einstein condensate (BEC) is formally equivalent to a dissipationless version of the so-called Landau–Lifshitz equation (LLE) for the magnetization dynamics in ferromagnets (see, e.g., 34 and references therein). For uniform configurations, in which the divergence of the spin-current is negligible, the equations take the form $\dot{\mathbf{s}} = (-\Omega, 0, 2g_{ss}s_z/\hbar) \times \mathbf{s}$, which are also called Bose–Josephson junction (BJJ) equations (35). In terms of the relative magnetization $Z = s_z/n$ and of the relative phase ϕ_r, they can be written in the following form:

$$\dot{Z} = -\Omega\sqrt{1 - Z^2}\sin\phi_r, \qquad\qquad 27.$$

$$\dot{\phi}_r = \Omega Z\left(\Lambda + \frac{1}{\sqrt{1 - Z^2}}\cos\phi_r\right), \qquad\qquad 28.$$

where $\Lambda = \frac{2g_{ss}n}{\hbar\Omega}$. Depending on the initial condition and on the value of Λ, the BJJ equations exhibit a number of different dynamical regimes (we refer the reader to original theory in References 35 and 36 for a more comprehensive discussion). In the present context, it is useful to remember that the stationary points are characterized by $\phi_0 = 0$ or π and by the value Z_0 of the spin polarization. The value of Z_0 is different from 0 only for $|\Lambda| > 1$, with $Z_0 = \pm\sqrt{1 - \Lambda^{-2}}$. In the limit of small amplitude oscillations around equilibrium, the system is characterized by the frequency,

$$\omega_J^2 = \Omega^2\left(\Lambda\sqrt{1 - Z_0^2}\cos\phi_0 + \frac{1}{1 - Z_0^2}\right), \qquad\qquad 29.$$

which, in the absence of interactions ($\Lambda = 0$), reduces to $\omega_J = \Omega$.

The paramagnetic and ferromagnetic phases described in the previous sections correspond to the stationary solutions $\phi_0 = 0, Z_0 = 0$ and $\phi_0 = 0, Z_0 = \pm\sqrt{1 - \Lambda^{-2}}$, respectively. In both cases, the value $\hbar\omega_J$ coincides with the gaps of the spin elementary excitation for $k \to 0$. The stationary point $\phi_0 = \pi$ instead corresponds to a maximum of the Rabi energy (Equation 5) and gives rise to a dynamically unstable configuration, the excitation spectrum, which is derivable from the linear solutions (Equations 22–24) and becomes imaginary for some values of the momentum.

The existence of stationary points with $Z_0 \neq 0$ is at the origin of the celebrated self-trapping regime (35, 36). In such a regime, the polarization cannot change sign; i.e., if the majority of atoms is initially in one of the two spin states, this will be true during all the time evolution. The self-trapping configuration in which both the phase and the polarization oscillate is called 0 or π-mode, depending on the value of ϕ_0. More interesting are the so-called running phase modes, in which the phase keeps increasing. Running phase solutions exist only for $|\Lambda| > 2$, and in this case the phase space $Z - \phi$ is reminiscent of the angle–angular velocity phase space of a classical pendulum. In particular, there exists a separatrix, between the (Josephson) oscillating regimes—with zero time-average polarization—and the self-trapped regimes. The period of the oscillations diverges approaching the separatrix, and the effect is also named critical slowing down.

The various BJJ regimes have been experimentally investigated in detail both in the originally proposed (35) double-well potential geometry (37–41)—where the imbalance Z corresponds to the difference in the number of atoms in the right and in the left well—as well as in the internal Josephson configuration (26, 42), using Rabi coupled BECs.

It is worth mentioning that the dynamic instability of the $\phi_0 = \pi$ configuration is not relevant for most of the present-day experimental realizations of the BJJ equations. Indeed the atoms are usually trapped by tight confinements, so that the orbital degrees of freedom are frozen out and the BJJ equations properly describe the dynamics of the system.[2]

The instabilities occurring in extended systems, in which one should rather use the full Equations 22–24, are of the Cross–Hohenberg type (43) and are characterized by complex elementary excitations at rather well-defined momenta and whose energies have a vanishing or finite real part; for this reason they are called I_s (static) and I_o (oscillatory) instabilities, respectively (43).

In cold gases mixtures, pattern formation due to an I_s-type instability has been already observed in spin-1 mixtures by Sengstock's group (44, 45). A proposal to observe the instability I_o in coherently coupled gas has been put forward in Reference 46 by means of a sudden quench from the stable ($\phi_r = 0$) to the unstable ($\phi_r = \pi$) configuration.

Let us conclude this section by mentioning that though Rabi coupled gases have been used to simulate the BJJ equations, at the moment the simulation of the full LLE (Equation 24), in which one takes into account both the time and the position dependence of the spin density, has not been explored. One of the main reasons for this is the experimental difficulty in maintaining a low and stable Rabi coupling in large systems in order to reveal the interplay between the x and z components of the effective magnetic field **H** together with the position dependence of the spin density. However, very recently, the possibility of describing Rabi coupled gases with the LLE has been experimentally verified and used to study the effect of the critical slowing down of the Josephson dynamics at the separatrix between a region in the self-trapped regime and a region in the Josephson oscillation regime (47).

3.4. Topological Excitations: Relative Phase Domain Walls and Half-Quantum-Vortices

Further peculiar features exhibited by Rabi coupled mixtures concern the phenomena related to topological defects, like solitons and vortices, involving the relative phase of the two components. A remarkable example is the relative phase domain wall, which was originally identified by Son & Stephanov (48).[3] As we discuss later the existence of this soliton solution is deeply connected with the novel features exhibited by quantized vortices in the mixture. A simple description can be obtained in the paramagnetic phase of uniform matter, under the assumption that $\hbar\Omega \ll g_{ss}n \ll g_{dd}n$ (50). In this limit, both densities $n_\uparrow$ and $n_\downarrow$ can be regarded as uniform and equal, with the only important degrees of freedom being the phases of the two order parameters, or, even better, the total $\phi_d = \phi_\uparrow + \phi_\downarrow$ and the relative phase $\phi_r = \phi_\uparrow - \phi_\downarrow$. The energy of the system, apart from a constant term, then takes the form

$$E(\phi_d, \phi_r) = \frac{n}{2} \int d\mathbf{r} \left[\frac{\hbar^2}{4m} (\nabla\phi_d)^2 + \frac{\hbar^2}{4m} (\nabla\phi_r)^2 - \hbar\Omega\cos(\phi_r) \right], \qquad 30.$$

---

[2]In the case of coherently coupled BECs the only change in Equation 28 is $Z = (N_\uparrow - N_\downarrow)/N$ and $\Lambda = 2g_{ss}N\alpha/(\hbar\Omega)$ (with N_σ being the total atom in the state σ), $N = N_\uparrow + N_\downarrow$, and α being a constant that takes into account the shape of the wave function of the tightly trapped gas (see, e.g., 26).

[3]The same kind of solution also has been described in the context of two-band superconductors by Tanaka (49).
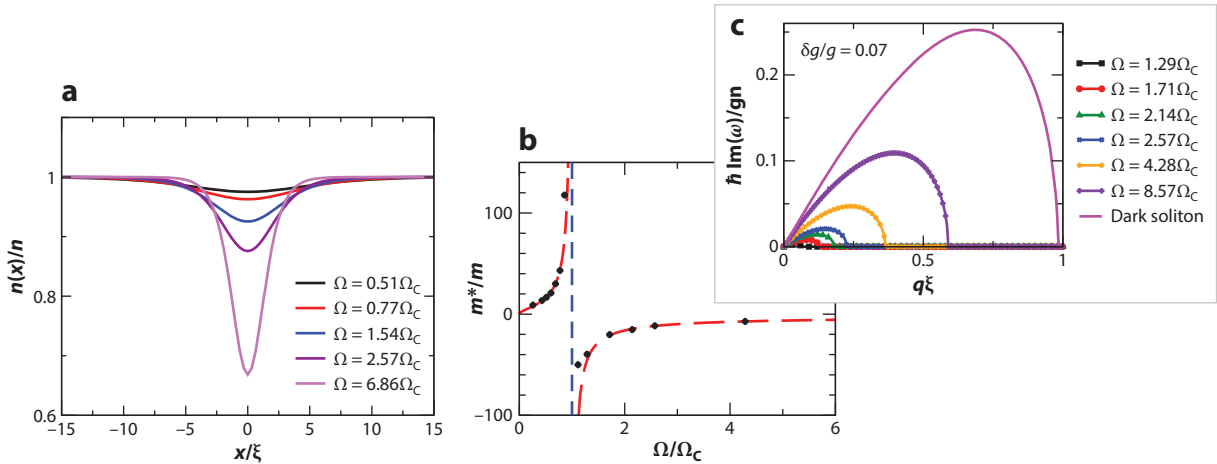
Figure 3

Relative phase domain wall obtained by solving coupled Gross–Pitaevskii equations as a function of the coupling Ω: (*a*) density profile, (*b*) effective mass, and (*c*) nonzero imaginary part of the spectrum yielding dynamic instability for $\Omega > \Omega_c$. The red dashed line in panel *b* corresponds to the analytical expression $m^* = m\xi_s n \frac{\sqrt{3\Omega\Omega_c}\pi^2}{4(\Omega-\Omega_c)}$ (50), whereas the black points correspond to the effective mass extracted from the excitation spectrum $\omega(q)$ for the transverse mode of the domain wall and its ground state energy E_{DW} using the relation $\lim_{q\to 0} \frac{\omega(q)}{q} = \sqrt{\frac{E_{DW}}{m^*}}$ (see 53). In all the panels, $g_{ss}/g_{dd} = 0.035$: typical value for ^{23}Na. Figure adapted with permission from Reference 53; copyright 2019 American Physical Society.

yielding the differential sine-Gordon equation $\hbar\nabla^2\phi_r = 2m\Omega\sin\phi_r$ (48, 49). For the domain wall solution, ϕ_r is a function of only one coordinate, say x, with the boundary condition that ϕ_r approaches a constant value as $x \to \pm\infty$. The trivial solution $\phi_\uparrow = \phi_\downarrow + 2\pi m = $ constant, with m integer, corresponds to the ground state solution of the Gross–Pitaevskii equations. A nontrivial solution, corresponding to an infinite domain wall located at $x = 0$, is given by (see, e.g., 51)

$$\phi_r(x) = 4\arctan\left[\exp(x/\xi_\Omega)\right], \qquad 31.$$

whose spatial variation is characterized by the Rabi healing $\xi_\Omega = \sqrt{\hbar/m\Omega}$. This stationary solution—which is a local minimum of the energy—connects two asymptotic ground states as x goes from $-\infty$ to $+\infty$ with relative phase equal to 0 and 2π in the two limits, respectively.

The solution (Equation 31) generates a counterflow current and accumulates the relative phase gradient in a small region of size ξ_Ω. The tension of the domain wall, i.e., its energy per unit area, is equal to $\sigma = (2\hbar)^{3/2}\sqrt{\Omega/m}$, revealing that the creation of a relative phase domain wall of infinite length would cost an infinite energy amount.

As already mentioned, Equation 31 is an approximation. However, the solution of the more general Gross–Pitaevskii equations for the stationary solitonic solution exhibits a similar equivalent phase pattern, but with a density dip near the wall as a consequence of the compressible nature of the gas. The dip increases with the increase of the Rabi coupling (52; as shown in **Figure 3a**), and for large values of Ω the central density vanishes, in close analogy with dark solitons.

An important question to discuss concerns the stability of the domain wall, which exhibits a deep difference with respect to the solitonic solution of a single-component BEC. In the latter case, the soliton is well known to suffer dynamic snake instability, unless one strictly works in one dimension (28). As pointed out by Son & Stephanov (48), for values of Ω below a critical value Ω_c, the domain wall solution is instead dynamically stable even in 3D configurations. Under the assumption $\hbar\Omega, g_{ss}n \ll g_{dd}n$ the critical value takes the simple expression $\Omega_c = ng_{ss}/3$ (48).

The stability of the domain wall is the consequence of the positiveness of its effective mass (53, 54) whose dependence on the Rabi coupling is shown in **Figure 3b**. Close to Ω_c the effective mass exhibits a divergent behavior, whereas for larger values it becomes negative and the domain wall undergoes dynamical snake instability as a consequence of the appearance of an imaginary part in the excitation spectrum (see **Figure 3c**).

Let us now discuss the consequences of the relative phase domain wall on the structure of vortex lines and let us consider a hypothetical domain wall of finite length. Around its end points the relative phase must change by 2π, corresponding to the presence, at the end point of the domain wall, of a vortex line in one of the two components, which is usually called a half-quantum vortex (HQV). This reveals that HQVs cannot exist as isolated objects (55), but they are always linked to a domain wall, eventually ending with a second HQV of the same atomic species with opposite circulation or with an HQV of the other species with the same circulation, thereby forming a sort of vortex molecule. This situation—as already pointed out in Reference 48—has intriguing analogies with the quark confinement in the theory of strong interactions (56).

It is remarkable that the classical field theory presented here can give rise not only to the confinement of HQVs but also to the pair creation phenomenology typical of quantum chromodynamics. An HQV pair is indeed stable only if its size is smaller than a critical value (56). If the pair size is larger than this critical value, it decays into two (or more) composite objects (53, 56, 57). The actual decay mechanism depends on a number of parameters, in particular on the value of the Rabi coupling Ω. In **Figure 4**, we report the case of a domain wall created across a cloud trapped by a harmonic potential in which the density becomes smaller and smaller as one approaches the surface region. The figure reports the case of both a dynamically stable ($\Omega < \Omega_c$) and a dynamically unstable ($\Omega > \Omega_c$) configuration. In the former case, the decay mechanism is very slow, whereas in the latter one the snake instability proceeds in a very fast way. In both cases, the formation of the vortex pairs, after fragmentation of the domain wall, preserves the initial vanishing value of angular momentum (53).

To our knowledge there exists at the moment only a single experiment (58) reporting the observation of a vortex–domain wall composite object in cold atomic gases. Although it has been obtained in spin-1 mixtures, the observed configuration exhibits important analogies with the scenario described above for a spin-1/2 Rabi mixture.

4. SPIN–ORBIT COUPLED CONFIGURATIONS

In this section, we describe the quantum phases, the elementary excitations, and the superfluid properties of spin–orbit coupled BECs, emphasizing analogies and differences with respect to the Rabi coupled mixtures discussed in the previous section. Spin–orbit coupled BECs were first experimentally investigated in the pioneering papers by the Spielman team (59, 60), motivated by the possibility of generating synthetic gauge fields (see also 61–63). Experimental results for degenerate spin–orbit Fermi gases have also become available (64, 65). Theoretically, the study of SOC gases has been the object of extensive investigations in the past several years. For previous review papers, see References 66 and 67. From the many-body point of view particularly challenging features are exhibited by the so-called ST phase, where first important supersolid effects have already been identified experimentally (68, 69).

4.1. Single-Particle Excitation Spectrum

A discussion of SOC in BEC systems naturally starts from the study of the excitation spectrum of the single-particle Hamiltonian (Equation 3). The deep modifications induced by SOC on the single-particle properties are in fact crucial to understanding the novel many-body features.
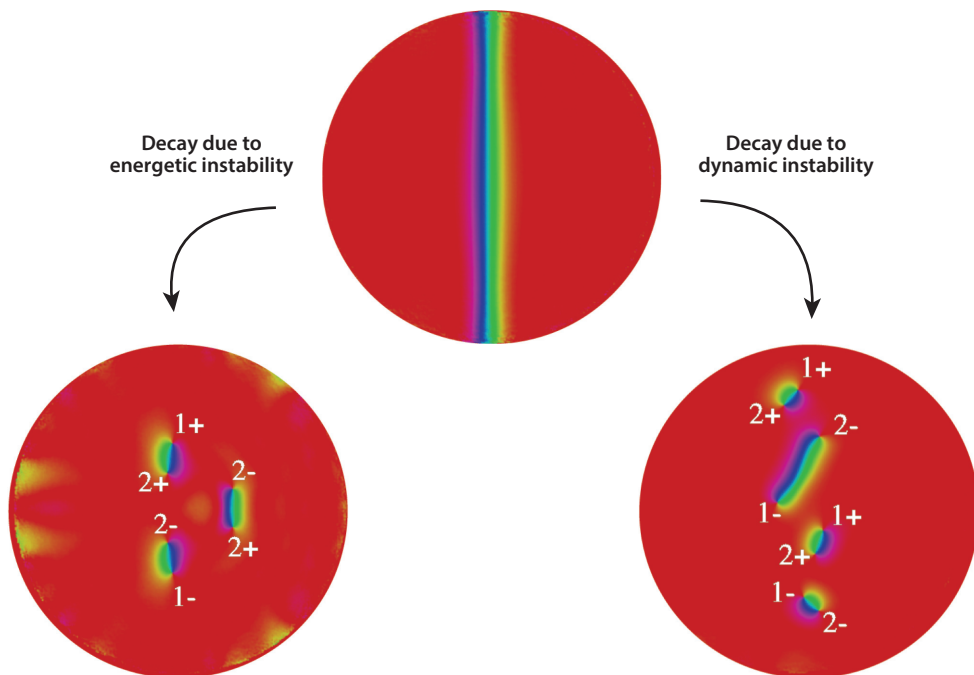
Figure 4

Phase profile of a long domain wall created at $t = 0$ (*upper panel*) across a two-dimensional Rabi coupled gas trapped by a harmonic potential $V(x, y) = 1/2 m\omega_{ho}^2(x^2 + y^2)$. The circle contour corresponds to the radius of the cloud, where the Thomas–Fermi density is zero. The domain wall decays (*left*) via energetic instability, after bending, into three composite objects or (*right*) via snake dynamic instability into four composite objects. The pairs consist of either vortices with the same circulation in both components ($1\pm, 2\pm$), or vortices with opposite circulation in one of the two component ($2\pm, 2\mp$). For more details see References 53 and 56.

In uniform matter, where the canonical momentum **p** is a good quantum number, the eigenvalues of Equation 3 are given by

$$\epsilon_\pm(\mathbf{p}) = \frac{p_x^2 + p_\perp^2}{2m} + E_r \pm \hbar\sqrt{\left(\frac{k_0 p_x}{m} - \frac{\delta}{2}\right)^2 + \frac{\Omega^2}{4}}, \qquad 32.$$

where $E_r = (\hbar k_0)^2/2m$ is the recoil energy and $p_\perp^2 \equiv p_y^2 + p_z^2$. The dispersion exhibits a typical double-band structure, reflecting the spinor nature of the configuration. Most interestingly, the dispersion is characterized by the occurrence of a double minimum for small Ω and δ, with the possibility of hosting BEC in single-particle states with $p_x \neq 0$. For large values of Ω (much larger than the recoil energy E_r), the lower branch exhibits a single-minimum structure of the form

$$\epsilon(\mathbf{p}) \rightarrow \frac{p_\perp^2}{2m} + \frac{1}{2m}(p_x + \hbar k_0 \delta/\Omega)^2 + \text{constant}. \qquad 33.$$

By introducing a space dependence in the detuning δ of the form $\delta = \alpha y$, the new gauge field in Equation 33 is responsible for an effective uniform magnetic field $B = \alpha \hbar k_0/\Omega$, oriented along the z-direction. This possibility was implemented experimentally in the pioneering work (59) to generate an effective Lorentz force, which was responsible for the appearance of quantized vortices in BEC gases (see **Figure 5**).
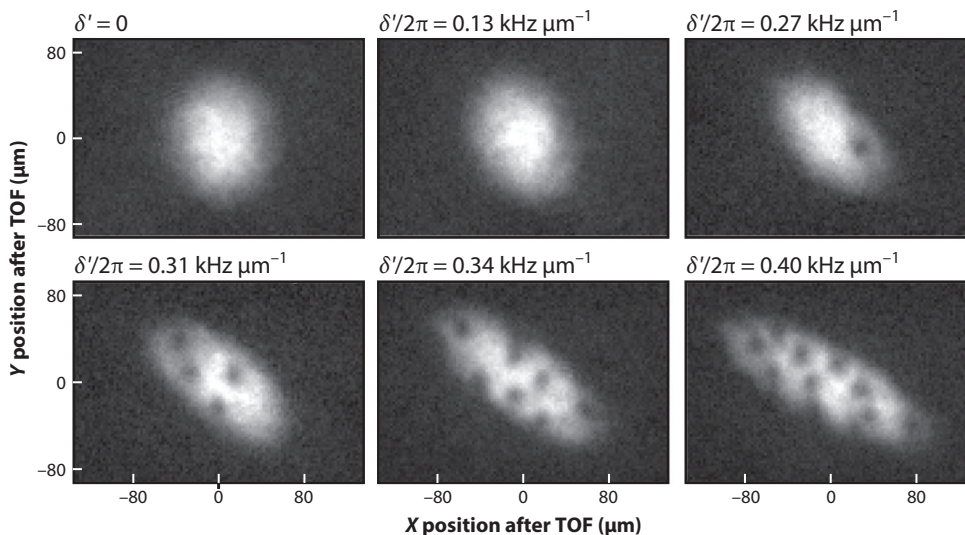
Figure 5

Appearance of vortices in a trapped spin-orbit-coupled Bose–Einstein condensate containing $N = 1.4 \times 10^5$ Rb atoms, at different detuning gradients. Figure adapted with permission from Reference 59; copyright 2009 Nature (**https://www.nature.com**). Abbreviation: TOF, time of flight.

In the case of vanishing detuning δ, which the single-particle dispersion (Equation 32) exhibits, for $\Omega < 4E_r$, two symmetric minima at quasi-momentum $p_x = \pm\hbar k_1$ with $k_1 = k_0\sqrt{1 - (\hbar\Omega/4E_r)^2}$. For larger values of Ω, the dispersion instead exhibits a single minimum at $p_x = 0$. It is also worth discussing the behavior of the effective mass $1/m^* = d^2\epsilon/dp_x^2$ of particles moving along the x direction. Near the minima one finds (70)

$$\frac{m}{m^*} = 1 - \left(\frac{\hbar\Omega}{4E_r}\right)^2 \text{ for } \hbar\Omega < 4E_r \text{ and } \frac{m}{m^*} = 1 - \frac{4E_r}{\hbar\Omega} \text{ for } \hbar\Omega > 4E_r. \qquad 34.$$

The effective mass exhibits a divergent behavior at $\hbar\Omega = 4E_r$, when the double-well structure disappears and the dispersion takes a p_x^4 law near the minimum. It is also worth noticing that for $\hbar\Omega < 4E_r$ the effective mass can have negative values when one moves away from the minimum, because of the change in the curvature of the function $\epsilon(p_x)$. This effect is responsible for important nonlinear instabilities that were observed in the center of mass oscillation (71) as well as in the expansion of the gas, following the release of the trap (72).

4.2. Quantum Phases and the Role of Interactions

The role of SOC in weakly interacting BECs can be properly described employing the MF energy functional (Equation 4), providing a natural generalization of Gross–Pitaevskii theory for two coupled Bose–Einstein condensed gases. In the previous subsection, we discussed how the value of the Raman coupling Ω changes in a deep way the structure of the single-particle states. More importantly, interactions are responsible for the emergence of a new quantum phase, the so-called ST or supersolid phase, which has attracted much interest in the recent literature. Interactions modify the conditions for the values of Ω to make the various phases energetically favorable. Choosing a vanishing detuning $\delta = 0$, one identifies the following quantum phases (see, e.g., 67).

4.2.1. Zero momentum (ZM) phase. For $\hbar\Omega > 4E_r - 2g_{ss}n$ the system occupies the $p_x = 0$ single-particle state. This phase is analogous to the paramagnetic phase discussed for Rabi coupled BEC. It exhibits nontrivial features concerning the magnetic, dynamic, and superfluid properties. For example, the magnetic susceptibility can be expressed as (73)

$$\chi_{ZM} = \frac{2}{\hbar\Omega - (4E_r - 2g_{ss}n)}, \qquad 35.$$

and it exhibits a divergent behavior as one approaches the transition to the plane wave phase at $\hbar\Omega = 4E_r - 2g_{ss}n$ and reduces to Equation 12 for $E_r = \hbar^2 k_0^2/2m = 0$.

4.2.2. Plane wave phase. As the value of the coupling Ω is lowered below $4E_r - 2g_{ss}n$, the system enters the so-called plane wave (PW) phase, in which the gas no longer occupies the $p_x = 0$ single-particle state but rather states with nonvanishing canonical momentum $p_x = \pm\hbar k_1$ that can be written in the form

$$\Psi_+ \equiv \sqrt{n} \begin{pmatrix} \cos\Theta \\ -\sin\Theta \end{pmatrix} e^{ik_1 x}, \quad \Psi_- \equiv \sqrt{n} \begin{pmatrix} \sin\Theta \\ -\cos\Theta \end{pmatrix} e^{-ik_1 x}. \qquad 36.$$

Minimization of the energy with respect to k_1 yields the value $k_1 = k_0\sqrt{1 - \Omega^2/(4E_r - 2g_{ss}n)^2}$ for the wave vector, which renormalizes the noninteracting value k_0. The value of the spin polarization is fixed by k_1 through the relation $s_z = n\cos(2\Theta) = k_1/k_0$. Notice that k_1, and hence s_z, vanishes as one approaches the transition to the ZM phase, corresponding to a second-order phase transition. Because for $\delta = 0$ the energy associated with the macroscopic occupation of the two states (Equation 36) is the same, the choice between the two configurations is determined by a mechanism of spontaneous symmetry breaking, which is typical of ferromagnetic configurations. The typical bifurcation exhibited by the canonical momentum $\hbar k_1$ has been explicitly measured by the Spielman team (60). The magnetic polarizability can be easily calculated also in the PW phase, where one finds the result (73)

$$\chi_{PW} = \frac{(\hbar\Omega)^2}{(2E_r - g_{ss}n)[4(2E_r - g_{ss}n)^2 - (\hbar\Omega)^2]}, \qquad 37.$$

which diverges as one approaches the transition to the ZM phase. As discussed in the Rabi coupled case, when one approaches the transition from above or below, the values of χ differ by a factor of two, reflecting its second-order nature. If one sets $g_{ss} = 0$ in Equations 35 and 37, the magnetic polarizability turns out to be fixed by the effective mass introduced in Section 4.1 through the relation $4E_r\chi_M = m/m^* - 1$. The magnetic susceptibility has been experimentally extracted (74) in the ZM and PW phases, through the analysis of the relative amplitude of the spin and momentum variables measured after exciting the dipole oscillation (73). The extracted values agree well with the theoretical predictions given by Equations 35 and 37 (see **Figure 6**). Again, if $k_0 = 0$, the polarization s_z and Equation 37 reduce to the Rabi coupled ferromagnetic case, in which case the condition $g_{ss} < 0$ is required.

4.2.3. Stripe phase. In the absence of two-body interactions, the occupation of any combination of the two single-particle states (Equation 36) discussed above is energetically equivalent. The situation changes in the presence of interactions, and depending on the balance between the density and spin density components of the interaction terms entering the energy functional (4), the system prefers to occupy either the above single-particle states separately, corresponding to the PW configuration, or the linear combination $\Psi = (\Psi_+ + e^{i\phi}\Psi_-)/\sqrt{2}$. This latter configuration, often called stripe (ST) or supersolid configuration, becomes energetically advantageous
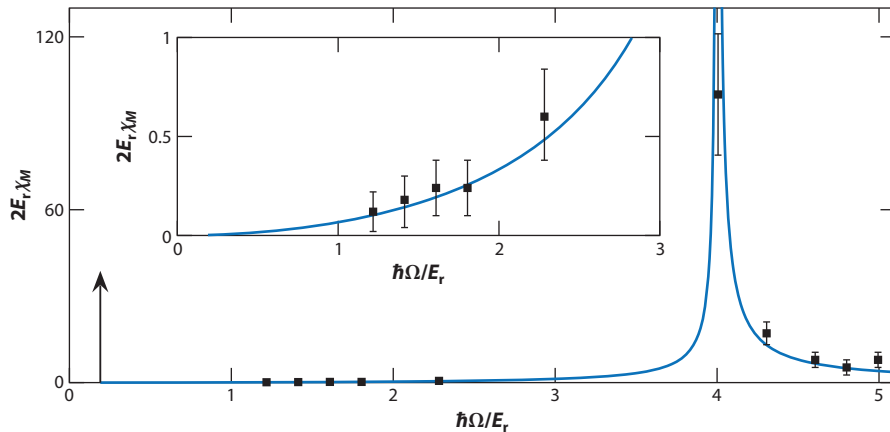
Figure 6

Magnetic susceptibility in the plane wave and zero momentum phases. Experimental data are extracted from spin and momentum amplitudes of the dipole oscillation (71). The inset is a blowup of the small $\hbar\Omega/E_r$ region. Theory is from Reference 73. The arrow indicates the transition to the ST phase. Figure adapted from Reference 67.

if the Raman coupling is smaller than the critical value (75),

$$\hbar\Omega_{cr} = 4E_r\sqrt{\frac{2\gamma}{1+2\gamma}} \ , \qquad\qquad 38.$$

where the relevant parameter $\gamma = g_{ss}/g_{dd}$ is fixed by the ratio between the spin and density interaction coupling constants. This result (Equation 38) holds for positive values of g_{ss} and under the condition $g_{dd}n, g_{ss}n \ll E_r$. The ST phase has vanishing spin polarization ($s_z = 0$) and is characterized by peculiar interference effects between the two components Ψ_+ and Ψ_-, giving rise, for small values of Ω, to density modulations of the form $n(\mathbf{r}) = \bar{n}\big[1 + (\hbar\Omega/4E_r)\cos(2k_1x + \phi)\big]$, with the actual position of the interference fringes being fixed by the value of the phase ϕ, which results from a mechanism of spontaneous breaking of translational symmetry. For this reason, this phase is also called the supersolid phase. Notice also that the space modulation of the density fringes is not uniquely fixed by k_0 because the value of $k_1 = k_0\sqrt{1 - \Omega^2/(4E_r + g_{dd}n)^2}$ differs from k_0, except in the $\Omega \to 0$ limit. The ST phase is also characterized by the peculiar behavior

$$\chi_{ST} = \frac{4(16E_r^2 - (\hbar\Omega)^2)}{32E_r^2 g_{ss}n - (\hbar\Omega)^2(g_{dd} + 2g_{ss})n} \qquad\qquad 39.$$

of the magnetic polarizability, which exhibits a divergent behavior at the critical point (Equation 38). The result (Equation 39), similar to Equation 38, holds only if $g_{dd}n, g_{ss}n \ll E_r$.

In order to increase the contrast of fringes and to strongly reveal the peculiar effects exhibited by the ST phase it would be useful to increase the value of Ω. However, one should keep in mind that the value of Ω cannot exceed the critical value (Equation 38) above which the system enters the PW phase. This value is usually small because in the most familiar case of alkali atoms the coupling constants relative to the various hyperfine states are very close to each other, causing the small value of γ. However, it has been recently shown (69) that a rapid jump in the value of the Raman coupling can provide a way to effectively increase the value of the contrast. In this experiment, the jump was in fact slow compared to the gap between the two branches of the SOC dispersion but fast compared to many-body dynamics, which would bring the system into

equilibrium. As a result, this process simply magnifies the amplitude of the SOC stripes, making them visible.

The direct experimental observation of stripes in SOC gases using Bragg spectroscopy (68, 69) has provided some of the first evidence of the long-sought phenomenon of supersolidity, where the spontaneous breaking of gauge symmetry, yielding superfluidity, and of translational invariance, yielding crystallization, coexist simultaneously. In Reference 76, a method was proposed to increase the value of the critical Raman coupling in conditions of thermodynamic equilibrium, making the supersolid features of the ST phase more visible. The proposal is based on the effective reduction of the interspecies coupling constant $g_{\uparrow\downarrow}$, with the consequent increase of Ω_{cr}. It could be achieved by reducing the spatial overlap between the wave functions of the two spin components, for instance, with the help of a spin-dependent trapping potential separating the two components.

4.3. Elementary Excitations and Goldstone Modes

The elementary excitations of an SOC BEC can be obtained by solving the Bogoliubov equations, corresponding to the linearized version of the coupled Gross–Pitaevskii equation. In uniform matter, they are classified in terms of the wave vector $\mathbf{k}$ of the excitation. Similar to the case of the eigenvalues (Equation 32) of the single-particle Hamiltonian, the solutions of the Bogoliubov equations also exhibit a double band structure, reflecting the spinor nature of the wave function. A typical example of the low branch dispersion is shown in **Figure 7**, obtained in the PW phase, where the excitation spectrum measured using Bragg spectroscopy techniques (74) is reported. Some comments are in order here: (*a*) The lower branch exhibits a linear phonon regime
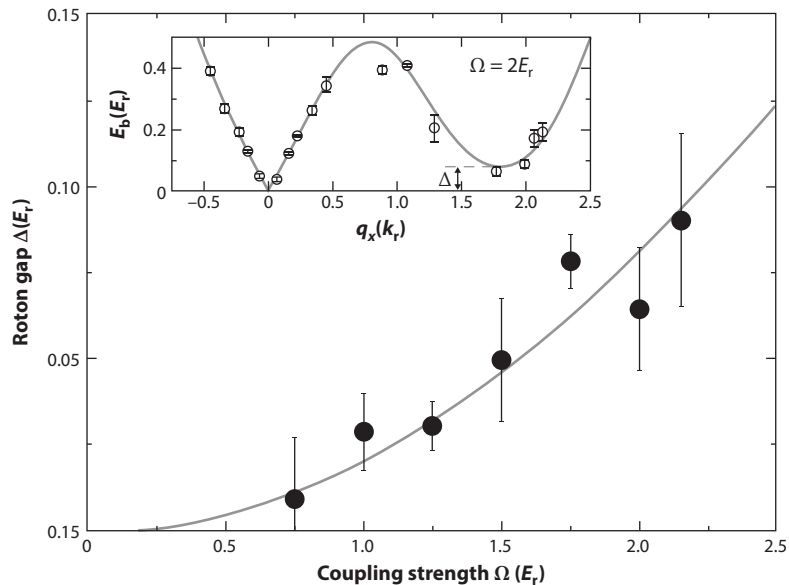
Figure 7

Lower branch of excitations in the plane wave phase of a spin–orbit coupled Bose–Einstein condensate revealing the phonon and roton excitations. Experimental data are from Reference 74. Theory is from Reference 76. Figure adapted with permission from Reference 74; copyright 2015 American Physical Society.

for small values of q_x, whose main features can be discussed using the hydrodynamic formalism; (b) the excitation spectrum violates the symmetry property $\omega(k_x) = \omega(-k_x)$ as a consequence of the simultaneous violation of parity and time-reversal symmetry exhibited by the spin–orbit Hamiltonian; and (c) the lower branch in the PW phase exhibits a typical rotonic structure for positive values of k_x (q_x in the figure). Most interestingly, the roton gap becomes smaller and smaller as one lowers the Raman coupling strength Ω, approaching the transition to the ST phase. Because the value of Ω_{cr} is very small, the transition to the ST phase is not visible in the figure. The agreement between experiments and theory is excellent, confirming the validity of the Gross–Pitaevskii MF approach in the study of the elementary excitations.

The region of small wave vectors and excitation frequencies can be appropriately described using the hydrodynamic representation in analogy with the description presented in Section 3.3 for Rabi coupled BECs. The hydrodynamic behavior of the system actually exhibits very peculiar features (77) in the PW and ZM phases. In uniform (or quasi-uniform) matter, where in the large wave-length limit one can neglect quantum pressure effects, the low-frequency oscillations satisfying the condition $\omega \ll \Omega$ are characterized by the locking of the relative phase: $\phi_r = \phi_\uparrow - \phi_\downarrow = 0$, which reduces the study of the Gross–Pitaevskii equation to the equations for the total density and phase $\phi_d = \phi_\uparrow + \phi_\downarrow$ and the spin density. These equations, in the linearized limit, take the following form:

$$\partial_t \delta n + \frac{1}{2m} \nabla \cdot (n \nabla \phi_d) - \frac{k_0}{m} \partial_x \delta s_z = 0, \qquad 40.$$

$$\partial_t \nabla \phi_d + 2\nabla(g\delta n) = 0, \qquad 41.$$

and

$$-\frac{k_0}{2m} n \partial_x \phi_d + \frac{\Omega}{2} \delta s_z = 0, \qquad 42.$$

where δn and δs_z are the fluctuations in the total density and in the spin density, respectively, taking place during the oscillation. For the sake of simplicity, we have assumed here that $g_{ss} = 0$ and considered the ZM phase characterized, at equilibrium, by the vanishing of the phase ϕ of the order parameter and of the spin density s_z. The first equation is the equation of continuity, which is deeply affected by SOC, reflecting the fact that the physical current is not simply given by the gradient of the phase as happens in usual superfluids, but contains a crucial spin-dependent term. This implies that even in the density channel the f-sum rule is not exhausted by the gapless phonon excitation but can be significantly affected by the higher-energy gapped states, which is caused by the Raman coupling. The second equation corresponds to the Euler equation and fixes the time dependence of the phase gradient of the order parameter. Finally, the third equation follows from the variation of the energy with respect to the spin density and is responsible for the hybridization between the density and spin density degrees of freedom in the propagation of sound (77). Notice that if one takes the $k_0 = \sqrt{2mE_r} \to 0$ limit, corresponding to the Rabi coupled configurations discussed in Section 3.2, the hybridization disappears and the phonon mode is a pure density wave. With respect to the hydrodynamic formulation presented in Section 3.3 for Rabi coupled mixtures, the hydrodynamic equations (Equations 40–42) cannot describe the dynamics of the relative phase, being applicable only to the regime of low-excitation frequencies, where ϕ_r is locked.

The linearized equations (Equations 40–42) can be rewritten in the following useful form:

$$\partial_t^2 \delta n = \frac{g}{m} [\nabla_\perp \cdot (n \nabla_\perp \delta n) + \frac{m}{m^*} \nabla_x (n \nabla_x \delta n)], \qquad 43.$$

where n is the equilibrium density, and we have introduced the effective mass $m/m^* = 1 - \Omega_c/\Omega$. One can show that Equation 43 holds also in the PW phase, taking place for $\Omega < \Omega_c$. In this case, the effective mass is given by $m/m^* = 1 - (\Omega/\Omega_c)^2$. In uniform matter, i.e., in the absence of external trapping, Equation 43 provides the phonon dispersion law $\omega = ck_x$ along the x direction, with $c^2 = gn/m^*$, revealing a strong reduction of the sound velocity in the vicinity of the second-order phase transition between the PW and the single-minimum phase, where the effective mass is much larger than the bare mass. If one includes the spin term proportional to g_{ss} in the hydrodynamic formalism, one finds that, in the PW phase, the sound velocity differs if sound propagates parallel or antiparallel to the direction fixed by the momentum transfer $\hbar k_0$ (67). The corresponding velocities c_+ and c_- satisfy the nontrivial relation $m\kappa c_+ c_- = (1 + 2E_r\chi)^{-1}$, with $1/\kappa = \partial\mu/\partial n$ being the inverse compressibility. This relation reflects the crucial interplay between magnetic effects and the propagation of sound in spin–orbit coupled BECs.

The hydrodynamic Equation 43 allows for analytic solutions also in the presence of harmonic trapping $V(\mathbf{r}) = m(\omega_x^2 x^2 + \omega_y^2 y^2 + \omega_z^2 z^2)$, where the Thomas–Fermi density profile, consistent with the choice $g_{ss} = 0$, has the spin–orbit independent form $n_{eq} = n_0(1 - x^2/R_x^2 - y^2/R_y^2 - z^2/R_z^2)$ and $\omega_x^2 R_x^2 = \omega_y^2 R_y^2 = \omega_z^2 R_z^2$ for positive values of n_{eq} and 0 otherwise. In this case, the solution of the hydrodynamic equations represents an immediate generalization of the results derived in Equation 78 in the absence of SOC, with the simple replacement of the trapping frequency ω_x with $\omega_x\sqrt{m/m^*}$. For example, the frequency of the center of mass oscillation along the x direction is expected to be strongly reduced in the vicinity of the transition between the PW and the ZM phases. This effect has been experimentally observed in Reference 71.

The dynamic behavior in the ST phase is particularly interesting because of the novel Goldstone branch introduced by the spontaneous breaking of translational invariance. In uniform matter, this branch approaches, as $\Omega \to 0$, the spin branch of standard quantum mixtures and is characterized, in the long wave vector limit, by the dispersion $\omega = \sqrt{g_{ss}n/mk}$. The velocity of the novel gapless mode becomes smaller and smaller as one approaches the transition to the PW phase and eventually vanishes at the spinodal point. Both the density and spin density branches propagating along the x direction exhibit a typical band structure characterized by the Brillouin wave vector k_1 (see **Figure 8**) and exhibit an important spin density hybridization effect for finite values of k_x. Remarkably, two gapless modes are also predicted to propagate along the direction parallel to the stripes, where the signal is classified in terms of the transverse wave vector $k_\perp$. Above the transition, only the density phonon branch survives, reflecting the fact that only the U(1) symmetry—associated with the total phase ϕ_d of the order parameter—is spontaneously broken.

The Goldstone modes in the ST phase have been recently theoretically investigated also in the presence of harmonic trapping (80, 81). In this case, one finds that, whereas in the PW and ZM phases the density and spin modes are fully hybridized, corresponding to the existence of a single gapless branch, in the ST phase one finds the emergence of a novel low-frequency excitation of spin nature (see **Figure 9**), whose experimental observation would represent further crucial evidence of supersolidity. The figure also shows the result $\omega_x/\sqrt{1 + k_0^2\chi_M}$, which provides a rigorous upper bound to the lowest mode excited by the dipole operator x (73). The bound is fixed by the magnetic susceptibility and accurately matches the center of mass frequency both in the PW and in the ZM phases. In the ST phase, the upper bound is instead significantly smaller than the frequency of the collective mode calculated by solving the time-dependent Gross–Pitaevskii equation after the sudden excitation of the center of mass oscillation. This suggests the existence of an excitation at lower frequency that is naturally interpreted as the analog of the $\omega = 0$ Goldstone mode of uniform matter, corresponding to the translational motion of the stripes.
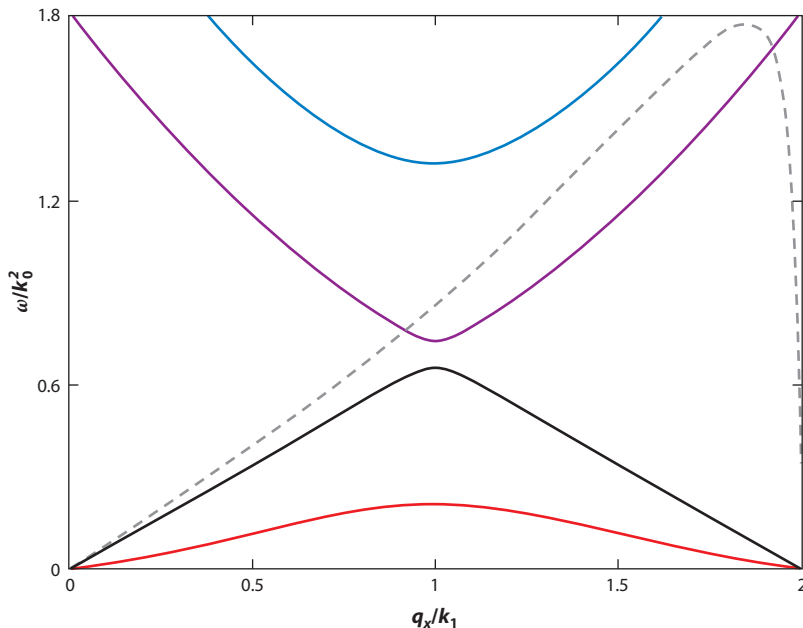
Figure 8

Lowest four excitation bands propagating along the x direction in the ST phase of a spin–orbit coupling
Bose gas ($\hbar = m = 1$). The lowest gapless branch is the novel Goldstone mode caused by the breaking of
translational invariance. Figure adapted with permission from Reference 79; copyright 2013 American
Physical Society.

4.4. Superfluidity and Moment of Inertia

Superfluidity is a key feature attracting considerable attention in the theoretical and experimental
studies of transport phenomena of quantum many-body systems at low temperature. It reflects
the property that only part (the normal component ρ_n) of a system is dragged by the wall of a
moving container, the superfluid component $\rho_s = \rho - \rho_n$ being able to move without friction.
Superfluidity exhibits novel features in spin–orbit coupled Bose gases, as a consequence of the
violation of Galilean invariance, which affects the usual Landau's criterion for superfluidity and
the stability conditions of the superfluid flow (70, 82, 83).

A useful definition of the normal density is obtained in terms of the response function of the
system to a transverse current perturbation. At zero temperature, one can write (84)

$$\frac{\rho_n}{\rho} = \frac{1}{N} \lim_{k \to 0} \left[\sum_{n \neq 0} \frac{|\langle 0|J_x^T(\mathbf{k})|n\rangle|^2}{E_n - E_0} + (\mathbf{k} \to -\mathbf{k}) \right], \qquad 44.$$

where $J_x^T(\mathbf{k})$ is the transverse current operator along the x direction (in the following, we choose
the wave vector $\mathbf{k}$ oriented along the y direction). As already pointed out in the previous sections,
a peculiarity of SOC is that the physical current is not simply given by the canonical contribution,
proportional to p_x, but it contains an additional spin component. As a consequence, the transverse
current operator takes the form $J_x^T(k_y) = \sum_k (p_{k,x} - k_0 \sigma_{k,z}) \exp(ik_y y_k)$. Because the transverse cur-
rent operator does not excite the gapless phonon mode, which is of longitudinal nature, the only
contribution to Equation 44 arises from the gapped part of the spectrum. In both the PW and
ZM phases, a single gapped branch is expected to occur. However, as $k \to 0$ limit, the transverse
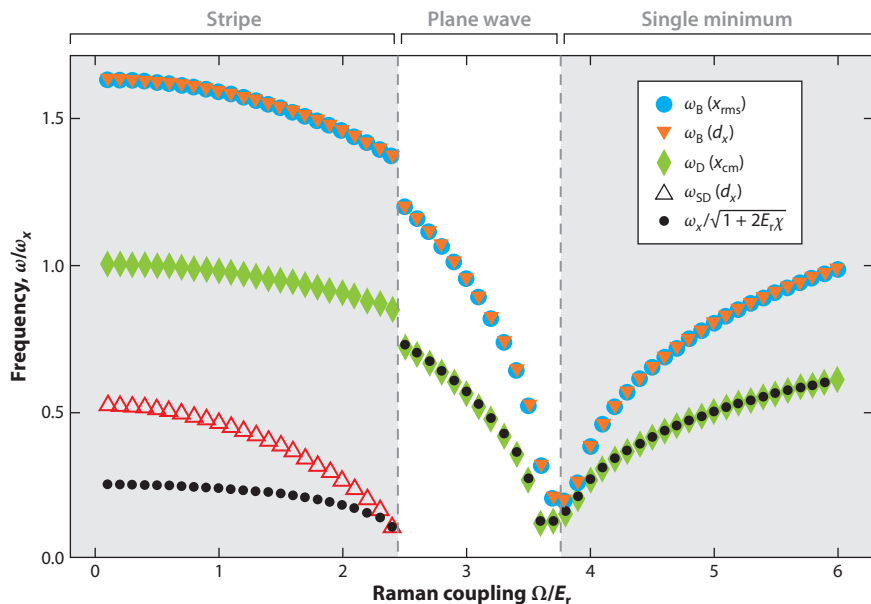
Figure 9

Goldstone modes of a spin–orbit coupling gas in an axially deformed harmonic trap. Below the transition between the ST and plane wave phases, one identifies, from top down: axial breathing mode, center of mass oscillation, and the novel spin dipole oscillation caused by the spontaneous breaking of translational symmetry. The black curve corresponds to the upper bound $\omega_x/\sqrt{1 + k_0^2\chi_M}$ to the lowest dipole oscillation, proving the occurrence of a lower frequency mode in the ST phase. Above the transition, the spin dipole mode is fully hybridized to the axial breathing mode. Figure adapted with permission from Reference 80; copyright 2021 American Physical Society.

contribution $|\langle 0|J_x^T(k_y)|n\rangle|^2$ to the sum (Equation 44), arising from the gapped state, coincides with the corresponding longitudinal one, which is simply obtained by replacing $\exp(ik_y y)$ with $\exp(ik_x x)$ in the definition of the current. Using sum rule arguments applied to the longitudinal channel, it is then possible to show (75) that the normal density fraction ρ_n/ρ is fixed by the contribution of the gapped branch to the f-sum rule and that the superfluid density satisfies the important relationship,

$$\frac{\rho_s}{\rho} = mc_+c_n\kappa = \frac{1}{1 + k_0^2\chi_M}, \qquad 45.$$

where c_+ and c_- are, respectively, the velocities of sound propagating parallel and antiparallel to the x direction of SOC, whereas κ is the compressibility of the gas. In the last equality, we have also used the relationship, derived in Reference 77, among the compressibility κ, the sound velocities $c_\pm$, and the magnetic susceptibility that was already discussed in Section 4.3. The effects of SOC near the transition between the PW and the ZM phases are striking, because of the divergent behavior exhibited by χ (see also **Figure 6**) showing that, even in configurations of uniform density, the superfluid density of a Bose–Einstein condensed gas at zero temperature is deeply modified as a consequence of the violation of the Galilean invariance of the Hamiltonian. It is also important to point out that quantum fluctuations have a negligible consequence on the depletion of the condensate (70), thereby revealing that the superfluid density crucially differs from Bose–Einstein condensation in these systems. The behavior of the superfluid density has also been the object of

theoretical calculations in the ST phase (85, 86), where the occurrence of density modulations and the consequent emergence of crystal-like effects is a further source of reduction of the ratio ρ_s/ρ.

A closely related quantity emphasizing the effects of superfluidity is the moment of inertia of a trapped gas. In atomic quantum gases, the moment of inertia has been the object of theoretical (87, 88) and experimental (89–91) works confirming the superfluid behavior of such systems. It is consequently interesting to discuss the consequences of SOC. The moment of inertia Θ_{inertia} around the z axis is defined as the linear response of the system to an external perturbation of the form $H_{\text{pert}} = -\Omega_{\text{rot}}L_z$, according to the definition $\Theta_{\text{inertia}} = \lim_{\Omega \to 0}\langle L_z \rangle/\Omega_{rot}$, which explicitly reveals the transverse nature of the response, in analogy with the definition (84) for the normal component of the density. Deviations of Θ_{inertia} from the classical rigid value $\Theta_{\text{rig}} = m\int d\mathbf{r}n(\mathbf{r})$ $(x^2 + y^2)$ then point out the consequences of superfluidity. The case of isotropic trapping in the plane of rotation is particularly interesting because in this case the constraint of irrotationality on the velocity field imposed by Bose–Einstein condensation in single-component configurations implies the vanishing of Θ_{inertia} (28). In SOC gases the situation is different because the angular momentum contains an additional crucial spin contribution: $L_z = \mathbf{r} \times \mathbf{p} + \hbar k_0 y\sigma_z$, thereby suggesting that even in the presence of isotropic density configurations in the x-y plane, causing the vanishing effect of the canonical contribution $\mathbf{r} \times \mathbf{p}$, the spin term can provide an important effect. The calculation of Θ_{inertia} can be carried out by either solving the coupled Gross–Pitaevskii equation in the presence of the constraint $-\Omega_{\text{rot}}L_z$ or using the hydrodynamic equations discussed in the previous section, with the addition of the term $-\hbar\Omega_{\text{rot}}k_0 y$ to Equation 42 for the spin density. The equation of continuity (Equation 40) is also modified by the new constraint, but with vanishing consequences in the isotropic case. Making the further simplifying assumption $g_{\text{ss}} = 0$, the solution of the hydrodynamic equations is analytic (92), and in the ZM phase the velocity field takes the rigid-body-like form $\mathbf{v} = (\boldsymbol{\Omega}_{\text{rot}} \times \mathbf{r})\Omega_{\text{cr}}/(2\Omega - \Omega_{\text{cr}})$, yielding the value

$$\Theta_{\text{inertia}} = \Theta_{\text{rig}}\frac{\Omega_{\text{cr}}}{2\Omega - \Omega_{\text{cr}}} \qquad 46.$$

for the moment of inertia. In the PW phase, one should simply replace the quantity $\Omega/(2\Omega - \Omega_{\text{cr}})$ with $\Omega^2/(2\Omega_{\text{cr}}^2 - \Omega^2)$. Remarkably, at the transition between the two phases ($\Omega = \Omega_{\text{cr}}$), the moment of inertia takes the rigid value, consistent with the result (45) discussed above for the superfluid density, which exactly vanishes at the transition. The above results are confirmed by the numerical solution of the Gross–Pitaevskii equation (93) and suggest that the inclusion of the detuning $y\sigma_z$ could be employed to provide the experimental measurement of the moment of inertia in configurations characterized by isotropic confinement in the x-y plane.

For values of Ω_{rot} greater than a critical value, the Gross–Pitaevskii equation reveals the existence of an energetic instability, resulting in the formation of quantized vortices. This confirms the efficient role played by the inclusion of the y dependence of the detuning to generate nontrivial rotational effects, as experimentally proven in the seminal paper, Reference 59, and theoretically discussed in References 93 and 94.

5. CONCLUSIONS AND PERSPECTIVES

In this paper, we have reviewed some key features exhibited by coherently coupled quantum mixtures of BECs, providing a combined discussion of Rabi and spin–orbit configurations in $S = 1/2$ spinor mixtures. The emerging scenario emphasizes the rich variety of phenomena exhibited by these systems, including new quantum phases and intriguing features of the elementary excitations and the Goldstone modes, as well as challenging phenomena, like the internal Josephson effect, novel solitonic configurations, and supersolidity. The discussion of these phenomena has explicitly pointed out the crucial role played by the symmetries of the underlying Hamiltonians. It has also

shown that the theoretical predictions and the comparison with the available experiments, carried out in mixtures of ultracold atomic gases, confirm that MF formalism, based on the use of Gross–Pitaevskii theory, is a useful starting point for the understanding of the main features exhibited by these systems. At the same time, a series of important questions still remain to be explored and understood from both theoretical and experimental points of view. Several specific questions have been discussed in various sections of the paper. More general open issues, not discussed in this review, include, among others, the study of thermal effects and the interplay between quantum and thermodynamic phase transitions, the crucial role of quantum fluctuations in lower dimensions, and the novel features exhibited by spinor quantum mixtures with $S \geq 1$.

DISCLOSURE STATEMENT

The authors are not aware of any affiliations, memberships, funding, or financial holdings that might be perceived as affecting the objectivity of this review.

ACKNOWLEDGMENTS

LITERATURE CITED

1. Anderson MH, Ensher JR, Matthews MR, Wieman CE, Cornell EA. 1995. *Science* 269(5221):198–201
2. Davis KB, Mewes MO, Andrews MR, van Druten NJ, Durfee DS, et al. 1995. *Phys. Rev. Lett.* 75(22):3969–73
3. Myatt CJ, Burt EA, Ghrist RW, Cornell EA, Wieman CE. 1997. *Phys. Rev. Lett.* 78(4):586–89
4. Edwards DO, Brewer DF, Seligman P, Skertic M, Yaqub M. 1965. *Phys. Rev. Lett.* 15(20):773–75
5. Baym G, Pethick C. 1978. In *The Physics of Liquid and Solid Helium*, *Part II*, ed. KH Bennemann, JB Ketterson, pp. 1–122. New York: John Wiley & Sons
6. Bychkov YA, Rashba EI. 1984. *J. Phys. C: Solid State Phys.* 17(33):6039–45
7. Dresselhaus G. 1955. *Phys. Rev.* 100(2):580–86
8. Lavoine L, Hammond A, Recati A, Petrov D, Bourdel T. 2021. *Phys. Rev. Lett.* 127(20):203402
9. Petrov DS. 2015. *Phys. Rev. Lett.* 115(15):155302
10. Cappellaro A, Macrì T, Bertacco GF, Salasnich L. 2017. *Sci. Rep.* 7(1):13358
11. Sachdeva R, Tengstrand MN, Reimann SM. 2020. *Phys. Rev. A* 102(4):043304
12. Sánchez-Baena J, Boronat J, Mazzanti F. 2020. *Phys. Rev. A* 102(5):053308
13. Barbiero L, Abad M, Recati A. 2016. *Phys. Rev. A* 93(3):033645
14. Bornheimer U, Vasić I, Hofstetter W. 2017. *Phys. Rev. A* 96(6):063623
15. Zhang S, Cole WS, Paramekanti A, Trivedi N. 2015. *Annu. Rev. Cold Atoms Mol.* 3:135–79
16. Hamner C, Zhang Y, Khamehchi MA, Davis MJ, Engels P. 2015. *Phys. Rev. Lett.* 114(7):070401
17. Kartashov YV, Konotop VV, Zezyulin DA, Torner L. 2016. *Phys. Rev. Lett.* 117(21):215301
18. Yamamoto D, Spielman IB, Sá de Melo CAR. 2017. *Phys. Rev. A* 96(6):061603
19. Cornell EA, Hall DS, Matthews MR, Wieman CE. 1998. *J. Low Temp. Phys.* 113(3):151–65
20. Abad M, Recati A. 2013. *Eur. Phys. J. D* 67:148
21. Goldstein EV, Meystre P. 1997. *Phys. Rev. A* 55(4):2935–40
22. Blakie PB, Ballagh RJ, Gardiner CW. 1999. *J. Opt. B: Quantum Semiclassical Opt.* 1(4):378–82

23. Matthews MR, Anderson BP, Haljan PC, Hall DS, Holland MJ, et al. 1999. *Phys. Rev. Lett.* 83(17):3358–61
24. Williams J, Walser R, Cooper J, Cornell EA, Holland M. 2000. *Phys. Rev. A* 61(3):033612
25. Sachdev S. 1999. *Quantum Phase Transitions*. Cambridge, UK: Cambridge Univ. Press
26. Zibold T, Nicklas E, Gross C, Oberthaler MK. 2010. *Phys. Rev. Lett.* 105(20):204101. **https://doi.org/10.1103/PhysRevLett.105.204101**
27. Nicklas E, Karl M, Höfer M, Johnson A, Muessel W, et al. 2015. *Phys. Rev. Lett.* 115(24):245301
28. Pitaevskii LP, Stringari S. 2003. *Bose–Einstein Condensation*. Oxford, UK: Oxford Sci. Publ.
29. Tommasini P, de Passos EJV, de Toledo Piza AFR, Hussein MS, Timmermans E. 2003. *Phys. Rev. A* 67:023606
30. Pethick CJ, Smith H. 2002. *Bose–Einstein Condensation in Dilute Gases*. Cambridge, UK: Cambridge Univ. Press
31. Recati A, Piazza F. 2019. *Phys. Rev. B* 99(6):064505
32. Mermin ND, Ho TL. 1976. *Phys. Rev. Lett.* 36(11):594–97
33. Nikuni T, Williams JE. 2003. *J. Low Temp. Phys.* 133(5):323–75
34. Bar'yakhtar VG, Ivanov BA. 2015. *Low Temp. Phys.* 41(9):663–69
35. Smerzi A, Fantoni S, Giovanazzi S, Shenoy SR. 1997. *Phys. Rev. Lett.* 79(25):4950–53
36. Raghavan S, Smerzi A, Fantoni S, Shenoy S. 1999. *Phys. Rev. A* 59(1):620–33
37. Albiez M, Gati R, Fölling J, Hunsmann S, Cristiani M, Oberthaler M. 2005. *Phys. Rev. Lett.* 95(1):010402
38. Schumm T, Hofferberth S, Andersson LM, Wildermuth S, Groth S, et al. 2005. *Nat. Phys.* 1(1):57–62
39. Levy S, Lahoud E, Shomroni I, Steinhauer J. 2007. *Nature* 449(7162):579–83
40. Trenkwalder A, Spagnolli G, Semeghini G, Coop S, Landini M, et al. 2016. *Nat. Phys.* 12(9):826–29
41. Spagnolli G, Semeghini G, Masi L, Ferioli G, Trenkwalder A, et al. 2017. *Phys. Rev. Lett.* 118(23):230403
42. Nicklas E, Strobel H, Zibold T, Gross C, Malomed BA, et al. 2011. *Phys. Rev. Lett.* 107(19):193001
43. Cross MC, Hohenberg PC. 1993. *Rev. Mod. Phys.* 65(3):851–1112
44. Matuszewski M. 2010. *Phys. Rev. Lett.* 105(2):020405
45. Kronjäger J, Becker C, Soltan-Panahi P, Bongs K, Sengstock K. 2010. *Phys. Rev. Lett.* 105(9):090402
46. Bernier NR, Dalla Torre EG, Demler E. 2014. *Phys. Rev. Lett.* 113(6):065303
47. Farolfi A, Zenesini A, Trypogeorgos D, Mordini C, Gallemì A, et al. 2021. *Nat. Phys.* 17:1359–63
48. Son DT, Stephanov MA. 2002. *Phys. Rev. A* 65(6):063621
49. Tanaka Y. 2001. *Phys. Rev. Lett.* 88(1):017002
50. Qu C, Tylutki M, Stringari S, Pitaevskii LP. 2017. *Phys. Rev. A* 95(3):033614
51. Tabor M. 1989. *Chaos and Integrability in Nonlinear Dynamics*. New York: John Wiley & Sons
52. Usui A, Takeuchi H. 2015. *Phys. Rev. A* 91(6):063635
53. Gallemí A, Pitaevskii LP, Stringari S, Recati A. 2019. *Phys. Rev. A* 100(2):023607. **https://doi.org/10.1103/PhysRevA.100.023607**
54. Ihara K, Kasamatsu K. 2019. *Phys. Rev. A* 100(1):013630
55. Kasamatsu K, Tsubota M, Ueda M. 2004. *Phys. Rev. Lett.* 93(25):250406
56. Eto M, Nitta M. 2018. *Phys. Rev. A* 97(2):023613
57. Tylutki M, Pitaevskii LP, Recati A, Stringari S. 2016. *Phys. Rev. A* 93(4):043623
58. Kang S, Seo SW, Takeuchi H, Shin Y. 2019. *Phys. Rev. Lett.* 122(9):095301
59. Lin YJ, Compton RL, Jiménez-García K, Porto JV, Spielman IB. 2009. *Nature* 462(7273):628–32
60. Lin YJ, Jiménez-García K, Spielman IB. 2011. *Nature* 471(7336):83–86
61. Galitski V, Spielman IB. 2013. *Nature* 494(7435):49–54
62. Dalibard J. 2016. In *Proceedings of the International School of Physics "Enrico Fermi" Course 191*, ed. M Inguscio, W Ketterle, S Stringari, G Roati pp. 1–61. Amsterdam: IOS Press
63. Galitski V, Juzeliūnas G, Spielman IB. 2019. *Phys. Today* 72(1):38–44
64. Wang P, Yu ZQ, Fu Z, Miao J, Huang L, et al. 2012. *Phys. Rev. Lett.* 109(9):095301
65. Cheuk LW, Sommer AT, Hadzibabic Z, Yefsah T, Bakr WS, Zwierlein MW. 2012. *Phys. Rev. Lett.* 109(9):095302
66. Zhai H. 2015. *Rep. Prog. Phys.* 78(2):026001
67. Li Y, Martone GI, Stringari S. 2015. *Annu. Rev. Cold Atoms Mol.* 3:201–50
68. Li JR, Lee J, Huang W, Burchesky S, Shteynas B, et al. 2017. *Nature* 543(7643):91–94

69. Putra A, Salces-Cárcoba F, Yue Y, Sugawa S, Spielman IB. 2020. *Phys. Rev. Lett.* 124(5):053605
70. Zheng W, Yu ZQ, Cui X, Zhai H. 2013. *J. Phys. B: Atom. Mol. Opt. Phys.* 46(13):134007
71. Zhang JY, Ji SC, Chen Z, Zhang L, Du ZD, et al. 2012. *Phys. Rev. Lett.* 109(11):115301
72. Khamehchi MA, Hossain K, Mossman ME, Zhang Y, Busch T, et al. 2017. *Phys. Rev. Lett.* 118(15):155301
73. Li Y, Martone GI, Stringari S. 2012. *Europhys. Lett.* 99(5):56008
74. Ji SC, Zhang L, Xu XT, Wu Z, Deng Y, et al. 2015. *Phys. Rev. Lett.* 114(10):105301. **https://doi.org/10.1103/PhysRevLett.114.105301**
75. Ho TL, Zhang S. 2011. *Phys. Rev. Lett.* 107(15):150403
76. Martone GI, Li Y, Stringari S. 2014. *Phys. Rev. A* 90(4):041604
77. Martone GI, Li Y, Pitaevskii LP, Stringari S. 2012. *Phys. Rev. A* 86(6):063621
78. Stringari S. 1996. *Phys. Rev. Lett.* 77(12):2360–63
79. Li Y, Martone GI, Pitaevskii LP, Stringari S. 2013. *Phys. Rev. Lett.* 110(23):235302. **https://doi.org/10.1103/PhysRevLett.110.235302**
80. Geier KT, Martone GI, Hauke P, Stringari S. 2021. *Phys. Rev. Lett.* 127:115301. **https://doi.org/10.1103/PhysRevLett.127.115301**
81. Chen L, Pu H, Yu ZQ, Zhang Y. 2017. *Phys. Rev. A* 95(3):033616
82. Zhu Q, Zhang C, Wu B. 2012. *Eur. Phys. Lett.* 100:50003
83. Ozawa T, Pitaevskii LP, Stringari S. 2013. *Phys. Rev. A* 87(6):063610
84. Baym G. 1968. In *Mathematical Methods in Solid State and Superfluid Theory*, ed. RC Clark, GH Derrick, pp. 121–56. Edinburgh, UK: Oliver & Boyd
85. Chen XL, Wang J, Li Y, Liu XJ, Hu H. 2018. *Phys. Rev. A* 98(1):013614
86. Sánchez-Baena J, Boronat J, Mazzanti F. 2020. *Phys. Rev. A* 101(4):043602
87. Guéry-Odelin D, Stringari S. 1999. *Phys. Rev. Lett.* 83(22):4452–55
88. Roccuzzo SM, Gallemí A, Recati A, Stringari S. 2020. *Phys. Rev. Lett.* 124(4):045702
89. Maragò OM, Hopkins SA, Arlt J, Hodby E, Hechenblaikner G, Foot CJ. 2000. *Phys. Rev. Lett.* 84(10):2056–59
90. Ferrier-Barbut I, Wenzel M, Böttcher F, Langen T, Isoard M, et al. 2018. *Phys. Rev. Lett.* 120(16):160402
91. Tanzi L, Maloberti JG, Biagioni G, Fioretti A, Gabbanini C, Modugno G. 2021. *Science* 371(6534):1162–65
92. Stringari S. 2017. *Phys. Rev. Lett.* 118(14):145302
93. Qu C, Stringari S. 2018. *Phys. Rev. Lett.* 120(18):183202
94. Radić J, Sedrakyan TA, Spielman IB, Galitski V. 2011. *Phys. Rev. A* 84(6):063604

Contents

Errata

An online log of corrections to *Annual Review of Condensed Matter Physics* articles may
be found at http://www.annualreviews.org/errata/conmatphys